HiSST: 3rd International Conference on
High-Speed Vehicle Science Technology
14 -19 April 2024, Busan, Korea

Numerical/Experimental Study Dual Injection in Supersonic Cross Flow

Sem de Maag[1], Jan Siemen Smink[2], Edwin T.A. van der Weide[2],
Harry W.M. Hoeijmakers[2] and Cornelis H. Venner[2]

Abstract

In order to minimize the length of supersonic-combustion ramjets (scramjets), injected fuel should mix rapidly with the supersonic cross flow. Tandem dual jet injection shows improved mixing performance over single jet injection. The present study comprises experimental work, using Schlieren flow visualisation in the supersonic wind tunnel of the University of Twente, as well as numerical simulation of the flow inside this wind tunnel, both at Mach number 1.6. The numerical simulation is based on (a) the Reynolds-averaged Navier Stokes (RaNS) equations for time-averaged flow for exploratory purposes; and (b) the time-resolved hybrid RaNS-LES, Delayed Detached Eddy Simulation (DDES) on a grid of 35M points. The Schlieren images from the experiments are analysed using a semi-automated post-processing procedure that generates an iso-incidence plot from which the time-averaged location of the upper boundary of the jet shear layer is determined. Subsequently an overall measure for the penetration depth of the main jet plume into the cross flow is found. The penetration depth is a function of two parameters (i) J, the ratio of the momentum of the jet and that of the cross flow and (ii) the nondimensionalized distance S between the dual jets. Based on Schlieren images from 24 (S,J)-combinations, the experimental work resulted in an empirical (scaling) similarity relation for the time-averaged location of the upper boundary of the jet plume and for the penetration depth. The empirical relationship has been validated by results from experiments for a further 21 (S,J)-combinations. The empirical relation shows that there is a region in the (S,J)-plane where the penetration depth is optimal: for given J there is an S for which the penetration is maximal. Numerical simulations facilitated the analysis of the time-dependent flow in great detail, using spatial distributions of vorticity, Mach number and total pressure. Furthermore, the spatial distribution of the density is used to generate numerical Schlieren images. These were run through the post-processing procedure for wind-tunnel Schlieren images. So far, DDES numerical simulations have been carried out for one representative (S,J)-combination. Its results were used to obtain insight in the flow phenomena that occur in the jet plume interacting with the cross flow. These results also validated the empirical similarity relation for the penetration depth of the jet plume.

(Keywords: Scram jet, jet in supersonic cross flow, Schlieren visualization, numerical simulation RaNS and DDES

Background

If the flow in the inlet of the combustor of ram-jet propulsion systems of airbreathing vehicles flying faster than Mach 6, would slow down to subsonic speed, temperatures, pressures and densities would be encountered that are too high for an efficient combustion [1]. Therefore, in order to facilitate efficient combustion, the inlet flow has to slow down from high supersonic speed to an acceptable lower supersonic speed. The ramjet is then called a scramjet, i.e., a supersonic combustion ramjet, see Fig. 1. In general vehicles equipped with scramjets achieve speeds from Mach 5 to Mach 12.

[1] *TNO, Defence, Safety & Security, PO Box 480, 2500 CL The Hague, The Netherlands, Sem.deMaag@TNO.nl*
[2] *University of Twente, Faculty Engineering Technology, Group Engineering Fluid Dynamics, PO Box 217, 7500 AE Enschede, The Netherlands, h.w.m.hoeijmakers@gmail.com*

In a scramjet, compressibility effects delay shear layer mixing [3]. In order to compensate for this effect long combustors are required to achieve a longer flow residence time and increase combustion efficiency. However, a longer combustor increases the skin friction drag in the combustor, therefore the overall drag of the engine is increased [4]. Thus, achieving faster mixing and combustion is of great

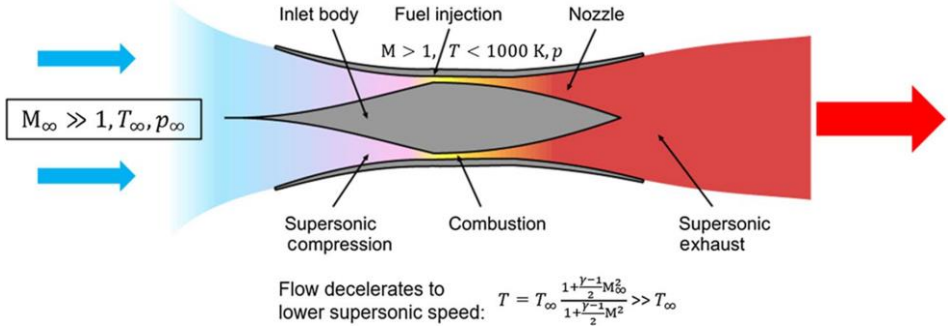

Fig 1. Supersonic combustion ramjet. By decelerating the flow from high supersonic speed to some lower supersonic speed, the temperature of the air entering the combustion chamber will remain below the ignition temperature of the fuel. Adapted from [2]

importance for scramjets because it allows a shorter combustor. To enhance mixing, injecting the fuel through one or two under-expanded sonic jets from the wall into the supersonic cross flow is an often-researched design solution.

Figure 2 shows the structure of the flow with injection of two, in tandem, under-expanded, sonic jets perpendicular to the supersonic cross flow. In front of each of the two jets, a three-dimensional bow shock forms. The bow shock in front of the jet decreases the momentum of the cross flow, which allows the jet to penetrate deeper into the cross flow [3].

The bow shock interacts with the flow in the subsonic part of the upstream boundary layer along the wall, which results in separation of the boundary layer upstream of the bow shock. The resulting increase in the boundary-layer thickness causes the formation of the so-called (oblique) separation shock that intersects the bow shock. The recirculating flow in the separated flow region forms a so-called horseshoe vortex wrapping like a scarf around the bow shock.

The interaction of the under-expanded sonic jet with the surrounding flow introduces a barrel shock closed by a Mach disc, inside the first portion of the plume of the jet. Furthermore, the jet will be forced to tilt from a normal direction at the exit of the jet to a direction almost parallel to the supersonic main stream. Due to the interaction with the main stream, the edge of the tilted jet deforms and rolls up in a counter-rotating pair of longitudinal vortices. The mixing of the fuel injected by the jets and the main stream depends strongly on these flow structures.

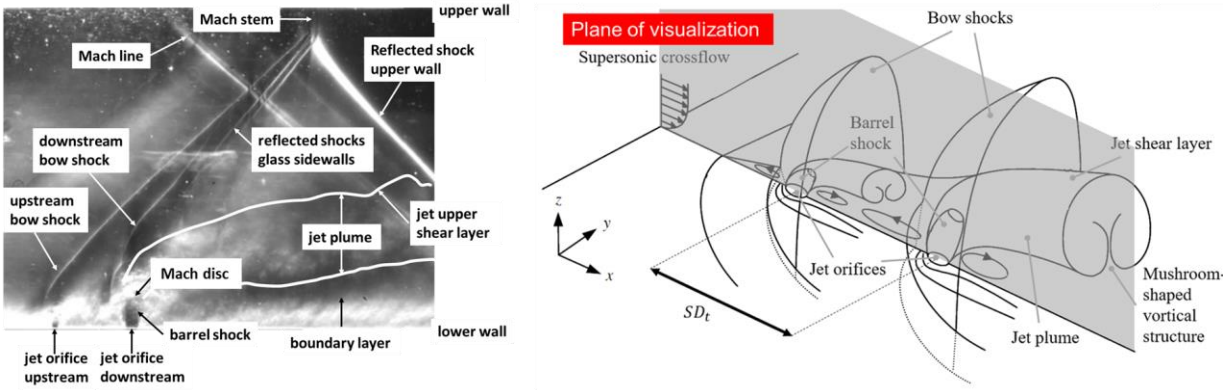

Fig 2. Left: Present Schlieren image tandem dual sonic jet injection in M_∞ = 1.6 air stream. D_1 = 1 mm, D_2 = 2 mm. J = 3.8 and S = 7.17. **Right**: Sketch of some flow features adapted from [5], [6]

The objective of the present paper is to study dual injection of (a tandem of) under-expanded sonic jets into a supersonic cross flow of Mach 1.6. The downstream jet, diameter D_2, is the main jet. The bow shock from the upstream jet, diameter $D_1 < D_2$, serves as a shield to slow down the flow upstream of the main jet. The result is an enhancement of the mixing of the fluid of the main jet and the fluid of the supersonic cross flow. For a given momentum ratio $J \equiv \rho_j U_j^2/(\rho_\infty U_\infty^2) = (\gamma_j p_j M_j^2)/(\gamma_\infty p_\infty M_\infty^2)$, the

dimensionless distance $S \equiv \Delta x/\sqrt{D_1^2 + D_2^2}$) between the two jets is the parameter that determines the effect of tandem dual injection on the penetration of the jet into the cross flow. The injection of a single jet, studied in an earlier study [7], is taken as reference.
The present study comprises experimental work, using Schlieren flow visualization in the test-section of the supersonic wind tunnel at the University of Twente and numerical simulation based on Reynolds-averaged Navier Stokes (RaNS) equations and of Delayed Detached Eddy Simulation (DDES) of the flow inside the test section of the wind tunnel. Numerical results are analysed in detail and compared with results from experiments using numerical Schlieren images.
The following sections describe
(i) Experimental set-up, wind tunnel and Schlieren flow-visualisation system;
(ii) Numerical method to solve RaNS equations and grid employed;
(iii) Numerical method based on DDES, a hybrid RaNS-LES (Large-Eddy Simulation), grid employed;
(iv) Results wind-tunnel experiments for 45 (*S,J*)-combinations, at a single Mach number of 1.6:
post-processing Schlieren images into iso-incidence plots that yields empirical similarity relations for time-averaged location of the upper boundary of the main jet plume, overall measure for jet penetration depth and optimal value of *S* for maximum penetration depth.
(v) Results numerical simulations based on RaNS equations. Exploratory numerical simulation for time-averaged turbulent flow in full-length wind tunnel, grid with 5M vertices;
(vi) Time-resolved results flow inside wind-tunnel test section, for 1000 time-steps of numerical simulations based on DDES on grid with 35M points. Detailed analysis of solution through numerical Schlieren images (density gradient), numerical shadowgraph images (Laplacian of density), spatial distributions of vorticity, Mach number and total pressure.
(vii) Conclusions on results and comparison of numerical results with experimental results.

Experimental Set-up

In the present paper the flow structures are visualized employing the Schlieren technique [8] as installed in the Supersonic Wind Tunnel at the University of Twente, see Fig. 3.

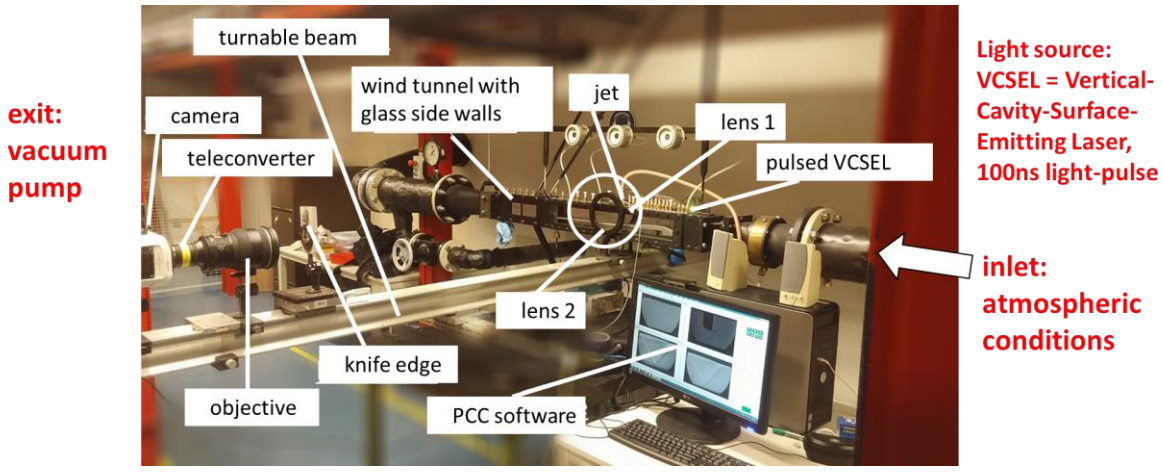

Fig 3. Set-up of continuous supersonic wind tunnel with Schlieren visualization system. Flow is from right to left. The atmospheric inlet, with silencer is not visible in the picture. The exit of the channel at the left is connected to a vacuum pump system

The supersonic facility is capable of achieving speeds up to Mach 1.7 continuously. In the present study the flow in the test section (between lens 1 and lens 2 of the Schlieren system) is set to Mach number 1.6. The test section measures $w \times h$ = 45mm×48mm perpendicular to the free stream.

The Schlieren system visualizes density gradients in a transparent medium. The light from the light source passes through lens 1, which results in a parallel bundle entering the test section through a high-quality-glass window. The variation in the density field results in refraction of the light, with the direction of the rays depending on the density gradient. The light then leaves the test section through the second glass window and subsequently passes through lens 2. Lens 2 focusses the (undisturbed) light into the focal point. The refracted light does not pass through the focal point and a part of this light meets a barrier, the "knife", located in the plane of the focal point. This results in a dark region

on the image. Another part of the refracted light will not be blocked by the knife, resulting in a lighter region on the image. These darker and lighter regions therewith visualize features that caused the refraction, i.e., the variation in the density field. Details of the Schlieren system, including the Vertical Cavity Surface Emitting Laser (VCSEL), are given in publications [9], [10] and [11] of earlier studies.

Numerical Simulations – Reynolds-Averaged Navier-Stokes Equations RaNS

Schlieren images of the flow field in the wind tunnel are created optically due to the nonuniform density field. Therefore, the Schlieren images of compressible flow visualize shock waves, expansions, contact surfaces, jets and boundary layers. A numerical equivalent, or rather approximation, coined "Numerical Schlieren" image, is the distribution of a derivative, e.g., in the x- or z-direction of the density field in an (x,z)-plane. In the present study this (x,z)-plane is chosen as the vertical plane, parallel to the main flow direction, which passes through the middle of the test section, designated as midplane. In this respect, the distribution of $\partial\rho/\partial z$ corresponds to the horizontal knife edge of the wind-tunnel Schlieren system, while $\partial\rho/\partial x$ corresponds to the vertical knife edge. Similarly, the distribution of the Laplacian $\nabla^2\rho$ in this plane corresponds, approximately, to a shadowgraph picture. The numerical Schlieren images and shadowgraphs, reveal most of the topology of the compressible flow inside the wind tunnel, which is augmented by detailed distributions of Mach number, total pressure, etc.

Though the experiments clearly show a transient flow behavior, for the initial, exploratory phase of the numerical part of the study, the equations solved are the steady Reynolds-averaged Navier-Stokes (RaNS) equations, in combination with the Spalart-Allmaras turbulence model. The open-source code SU2 [12], [13] has been used for these simulations. An unstructured computational grid has been generated that, in order to create an accurate boundary layer entering the test section, covers the entire wind-tunnel channel: the settling chamber, the throat, the supersonic diffusor, the test section and the exit of the tunnel, see Fig. 4.

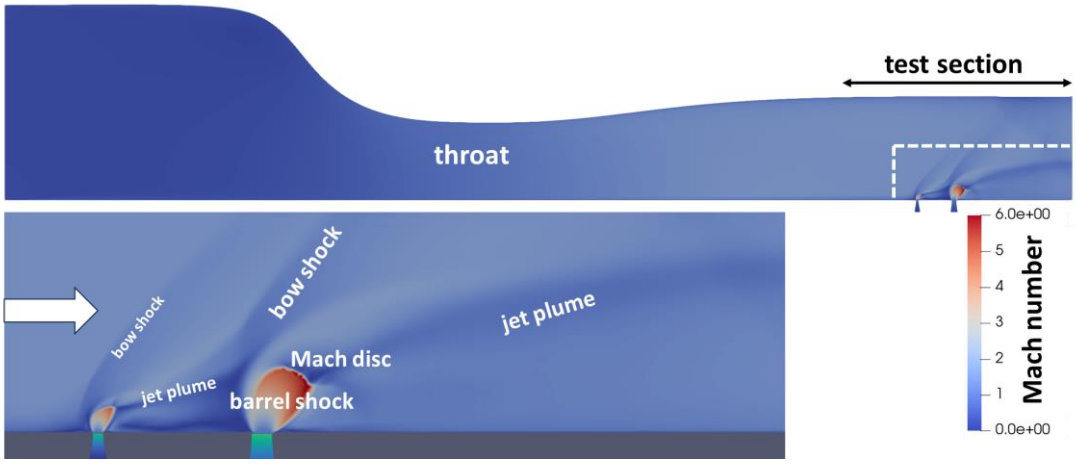

Fig 4. Top: computational domain inside wind tunnel. Flow is from left to right, from inlet via throat to test section, with dual-jet injection, to exit. **Lower left**: Enlargement of region of dual-jet injection. Colors indicate distribution of Mach number. M_∞ = 1.6, J = 3.8 and S = 7.17

The grid is composed of approximately 5 million vertices and 14 million control volumes. The chosen discretization is a vertex-based upwind finite-volume method in which the gradients of flow variables are computed using a weighted least-squares algorithm in combination with the Venkatakrishnan limiter and Roe's approximate Riemann solver for the advective fluxes. For the viscous terms a central discretization scheme has been employed. The iterative algorithm is a damped Newton method in which the linear system of algebraic equations, a result of an approximate linearization, is solved by a flexible GMRES algorithm. In the present application, this iterative algorithm reduces the residuals about three orders of magnitude before the residuals start to oscillate, indicating that the flow is indeed transient, even for the RaNS approximation.

Numerical Simulations – Delayed Detached Eddy Simulation DDES

In the present study, SU2 is also used to perform an unsteady flow analysis, at the same (S,J)-combination as the (S,J)-combination of the experiment, making use of a Delayed Detached Eddy Simulation (DDES). DDES is a hybrid Large-Eddy-Simulation (LES)/RaNS model of turbulent flow, developed by Spalart et al. [14], [15]. The DDES version is a further development of the original DES model, which

reduces the dependency of the solution on the computational grid. The model uses a RaNS formulation near the wall, but an LES formulation away from the wall. By using a RaNS formulation near the wall, the huge grid requirements of a fully wall-resolved LES are avoided, while still capturing the transient behavior of the turbulence. This is accomplished by modifying the original RaNS turbulence model, in this case the Spalart-Allmaras model [16], away from the wall. For more details see [14], [15].
The computational grid used for the simulation is an unstructured grid composed of tetrahedra, prisms, pyramids but mainly hexahedra. For the DDES numerical simulation, the computational domain comprises just the test section, not the full-length channel, as used for the RaNS numerical simulations in the preceding section. In order to reduce the size of the computational grid for the DDES simulations, the viscous effects on the top and side walls are neglected. Due to the absence of upstream influence in a supersonic flow, this simplification has no or a minimal impact on the flow in the region of interest, namely the region between the jets and the region above the wall downstream of the second orifice, the region where the main jet develops and the penetration of the main jet takes place.
Effects of the shorter upstream computational domain will occur primarily in the boundary layer along the walls, specifically the interaction of the boundary layer with the bow shock in front of the upstream jet. However, it is expected that this will have only a minor effect on the main jet and its penetration in the supersonic cross flow. Still, the total number of points is a respectable 35 million. An intersection of the grid with the (x,z)-plane in the middle of the channel is presented in Fig. 5, together with a close-up of the grid in the region of the two jets.

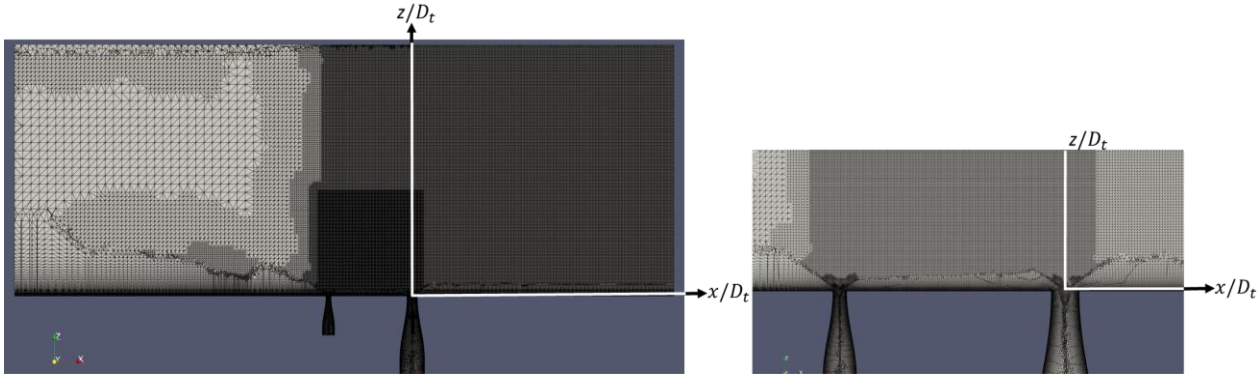

Fig 5. Midplane intersection of computational grid in test section wind-tunnel channel. **Left**: Full domain with 35M grid; **Right**: Close-up of part computational grid in region of tandem jet orifices. S = 7.17

The flow solver used for the simulation is the open-source code SU2 [13]. The simulation was initialized using a steady RaNS solution, followed by a restart using DDES, with a time step of 1 microsecond. The time integration scheme used is the second-order implicit backward Euler scheme, while a second-order upwind scheme is used for the spatial discretization using Roe's approximate Riemann solver. Due to the strong shock waves present the Wang [17] formulation of the Venkatakrishnan limiter is employed. To wash out the transients caused by the restart from the RaNS solution, 2000 time-steps were performed before the actual data was collected for another 1000 time-steps, i.e., for 1 millisecond in real time. This corresponds to roughly 8 test-section flow-through times based on the free-stream velocity. The set of nonlinear equations for every time step is solved using the dual-time stepping procedure in combination with an implicit Euler scheme, solving the linearized equations with two steps of GMRES. A total of 20 iterations were sufficient to converge the nonlinear equations.
The simulation itself was run on 180 cores (Xeon processors @ 2.30 GHz) and took approximately 50 hours. The size of the resulting data set is 5 TB, which was visualized using the open-source post processing tool ParaView [18].

Results Experimental Study

For the injection of dual sonic jets Schlieren visualization has been carried out for a number of conditions. Figure 6 presents, for J = 3.8, one sample Schlieren image for each value of S that has been investigated. These results show that for smaller values of S the shielding effect increases up to intermediate values of S for which the penetration height reaches a maximum. For still higher values of S, the shielding effect decreases again.
The present investigation employs, the largely automated, post-processing procedure developed by Smink [11], which for each (J,S)-combination can handle a relatively large number of images reliably.

The end result of the procedure, which manipulates light-intensity maps in the region of the jet plume, is the so-called iso-incidence plot, an example of which is given in Fig. 7. The iso-incidence plot is obtained from thirty consecutive images, 1 ms apart in time, considered for a specific (J,S)-combination. Then per pixel the number of times a feature (light intensity exceeding a threshold value) occurs is determined, which corresponds to a time-averaged quantity.

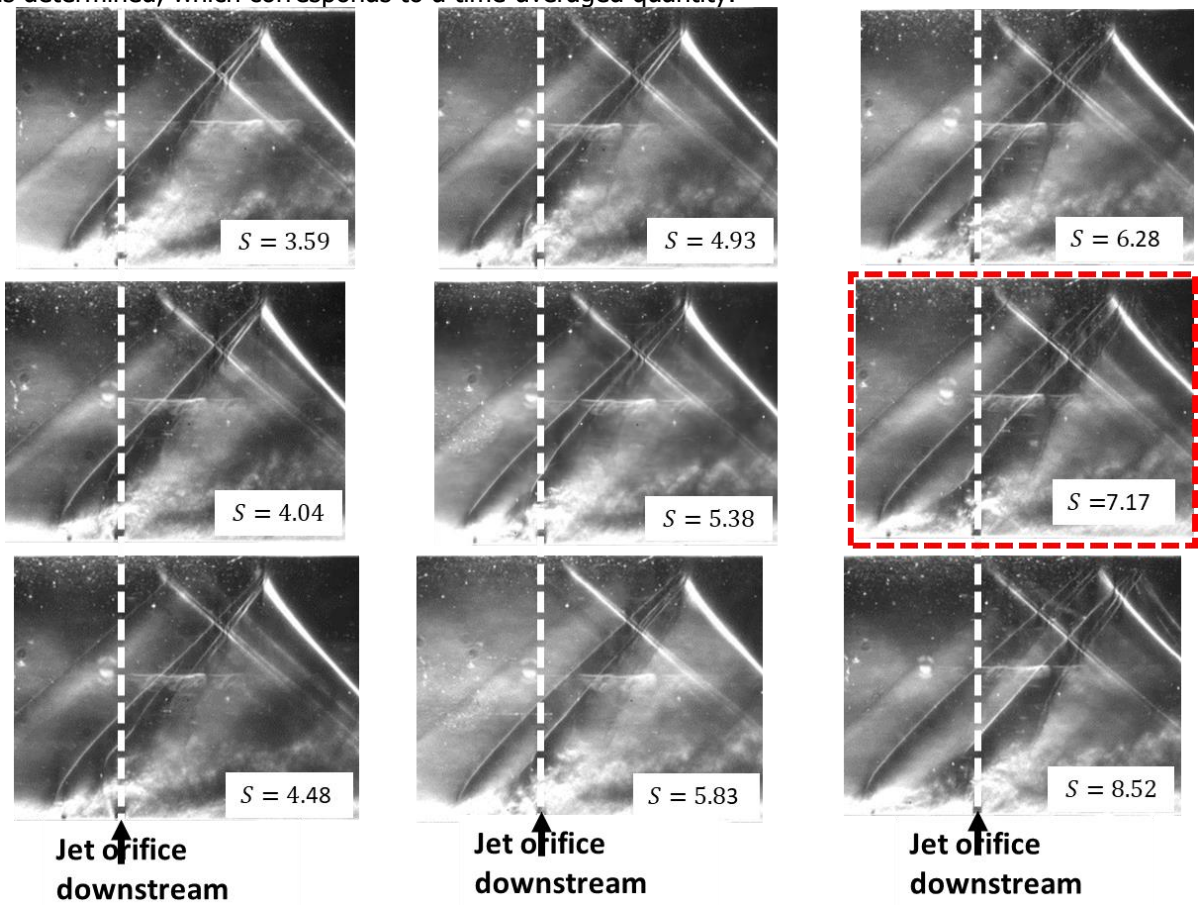

Fig 6. Schlieren images for $J = 3.8$, for range of values of S. For every (S,$J = 3.8$)-combination, one of the 30 images available is shown. $\mathrm{M}_c = 1.6,\ D_1 = 1\ \mathrm{mm}, D_2 = 2\ \mathrm{mm}.$ Red: Fig. 2, 4 and 7-16. Vertical dashed white line indicated location main orifice

At a specific location in the jet plume the color indicates the incidence, an integer between 0 and 30, revealing either largely stationary, or frequently-occurring, flow structures. For instance, in Fig. 7 the region just above the barrel shock indicates high values of the incidence (dark red color), because the Mach disc shows up at that location in almost all of the 30 images processed.

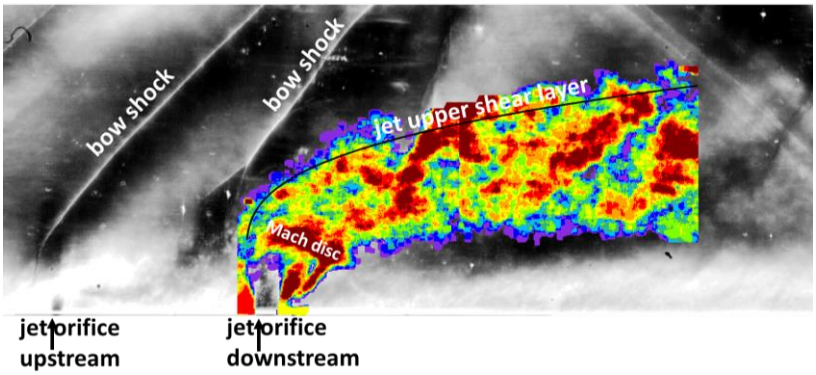

Fig 7. Iso-incidence plot obtained from 30 consecutive Schlieren images, 1 ms apart in time. Features inside jet are visualized as reddish islands of higher incidence, which represent stationary, or frequently-occurring features (Fig. 6 red dashed square: $J = 3.8$, $S = 7.17$, and $\mathrm{M}_c = 1.6, D_1 = 1\ \mathrm{mm}, D_2 = 2\ \mathrm{mm}$). Solid curve: similarity expression for time-averaged location upper edge jet shear layer, Eq. (1a)

The upper boundary of the region, with non-zero values of the incidence, represents the time-averaged upper edge of the plume, which in the present study is used as measure for the penetration depth of the jet. In previous work [19], presented at HiSST2022, the penetration depth has been found to satisfy an empirical relation that fits the data of all (*S,J*) combinations considered at $\mathrm{M}_c = 1.6$:

$$\frac{z}{D_t}\left(\frac{x}{D_t}; J, S\right) = 0.432J^{0.461}[2 + e^{-\frac{1}{2}\left[\frac{S-4.732J^{0.288}}{6.103J^{-0.521}}\right]^2}][\left\{\left(\frac{x}{D_t}\right) + 0.68\right\}^{0.333} + 0.80], \tag{1a}$$

with z/D_t is the (time-averaged) vertical penetration depth as function of the horizontal distance x/D_t from the center of the downstream jet orifice, for given *J*, i.e., the ratio of the momentum of the jet and that of the cross flow and *S*, the dimensionless distance between the two tandem orifices. An overall measure of the penetration depth of the upper jet shear layer of the plume, is the spatial average of Eq. (1a) from the center of the downstream edge of the main orifice at $x \approx 0.5D_t$ to $15D_t$ downstream. This yields:

$$\frac{z_{avg}}{D_t}(J, S) = 1.194J^{0.461}[2 + e^{-\frac{1}{2}\left[\frac{S-4.732J^{0.288}}{6.103J^{-0.521}}\right]^2}]. \tag{1b}$$

Because of the shielding effect of the jet from the upstream orifice, the penetration depth of the jet plume into the cross flow exceeds the penetration depth of a single jet configuration, at the same *J*, when the upstream jet is moved upstream, away from the primary jet. However, for large distances $S = \Delta x/D_t$, the shielding effect decreases and the penetration depth of the main jet plume decreases towards that of a single jet with the same D_t. Therefore, there is an optimum value of *S* for maximum penetration. It follows from Eq. (1b) that:

$$S_{opt}(J) = 4.732J^{0.288}, \text{ for which } \frac{z_{avg,opt}}{D_t}(J) = 3.582J^{0.461} \tag{1c}$$

The test case selected for the numerical study is: *J* = 3.8 and *S* = 7.17, close to $S_{opt}(3.8) = 6.95$, see red dashed box in Fig. 6.

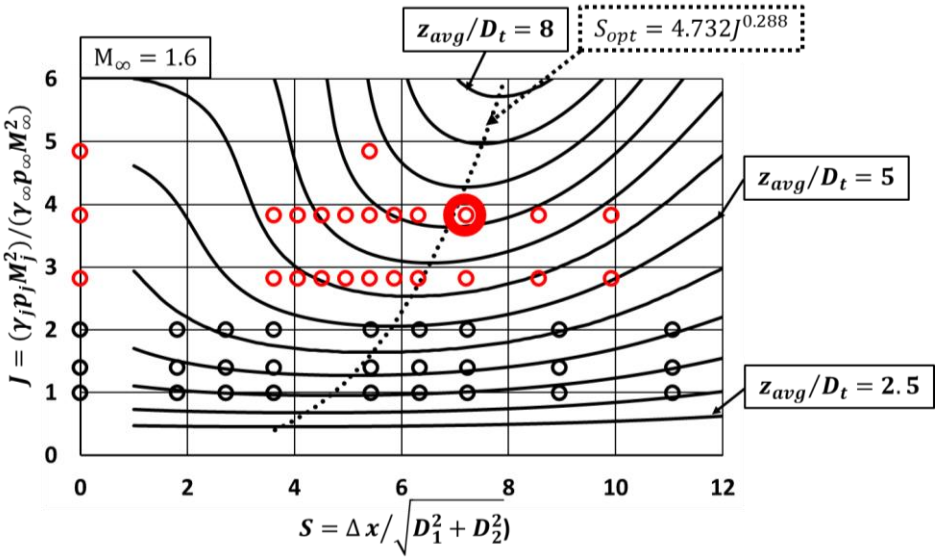

Fig. 8. (*S,J*)-parameter plane experimental study. Black open circles: Ref. [9], [10]. Red open circles: Ref. [11], [19]. Big red circle: Selected condition for RaNS and DDES numerical simulations. Solid black curves: iso-contours of z_{avg}/D_t, Eq. (1b) $z_{avg}/D_t = 2.5(0.5)8$. Dotted block line: $z_{avg,opt}/D_t$, Eq. (1c)

Fig. 8 provides an overview of the (*S,J*)-combinations for which Schlieren images have been obtained in the supersonic wind tunnel at the University of Twente. The data used to develop the empirical scaling relation for z/D_t, given in Eq. (1a), have been extracted from the Schlieren images based on the post-processing procedure described above, which utilizes iso-incidence plots like Fig. 7. The resulting empirical scaling relation, Eq. (1b), for the overall measure z_{avg}/D_t of the penetration depth, has been plotted in Fig. 8 as iso-contours, for values of z_{avg}/D_t between 2.5 and 8. The curve for the optimal value of *S*, equal to $S_{opt}(J)$ given in Eq. (1c), has also been plotted. Fig. 8 shows that the region in the (*S,J*)-plane for which the (*S,J*)-combination is optimal, becomes narrower with increasing strength *J* of the jets. This indicates that the choice of the parameters for the near-optimal (*S,J*)-combination becomes more critical.

Results Numerical Study - RaNS

Figure 4 presents for M_∞ = 1.6, J = 3.8 and S = 7.17, the distribution of the Mach number in the whole computational domain. At the entrance of the wind-tunnel channel the flow starts at atmospheric conditions, followed by acceleration of the flow in the converging part of the channel. Mach 1 is reached at the narrowest section, the throat. In the diverging part of the channel the flow accelerates to M_∞ = 1.6 at the test section. The flow induced by the dual-jet injection corresponds to the one sketched in Fig. 2. Note that in the sonic under-expanded jet the flow inside the Mach barrel expands to a Mach number exceeding 5. The flow passing through the Mach disc decelerates to Mach numbers just above 1, which is maintained inside the jet plume. In the RaNS solution, the flow inside the jet may be considered as a measure of the time-averaged flow, while the Schlieren images in Fig. 6 are snapshots, taken with illumination time of 100ns, much smaller than the characteristic time of the flow, which is of the order of microseconds.

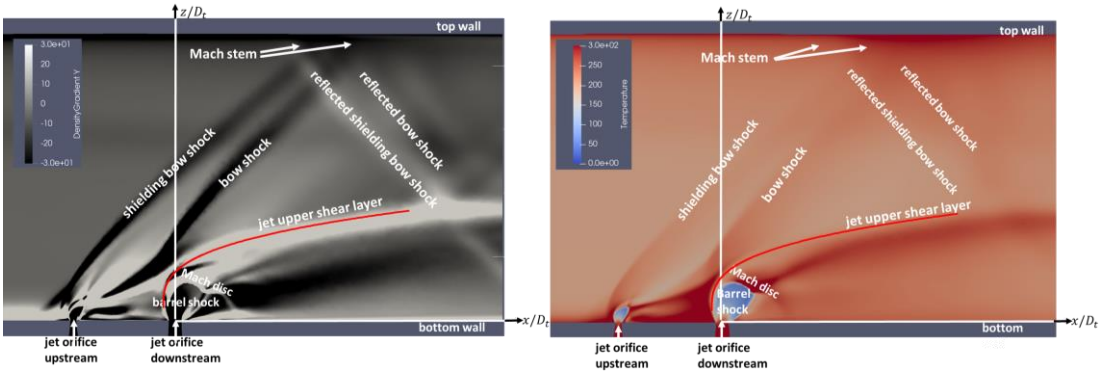

Fig 9. RaNS: **Left**: Numerical Schlieren image ($\partial\rho/\partial z$) of flow in (x,z)-plane (midplane) of wind tunnel, corresponding to image in red dashed box in Fig. 6. **Right**: Computed distribution temperature [K] in midplane. Red curve similarity relation Eq. (1a). M_∞ = 1.6, J = 3.8 and S = 7.17

Figure 9-left presents the numerical Schlieren image of the flow in the midplane of the test section, corresponding with the Schlieren image from the wind tunnel (Fig. 6, red square box). Fig. 9 – right presents the distribution of the temperature in the midplane. Flow features like shielding bow shock and bow shock from main jet interacting with the top wall, the separation shock, the barrel-shock/Mach-disc of the injection jets, boundary layers and the jet are resolved, though not as a snapshot but as some time-averaged image. Note that due to the strong expansion inside the barrel shock the temperature drops to values below 100 K.

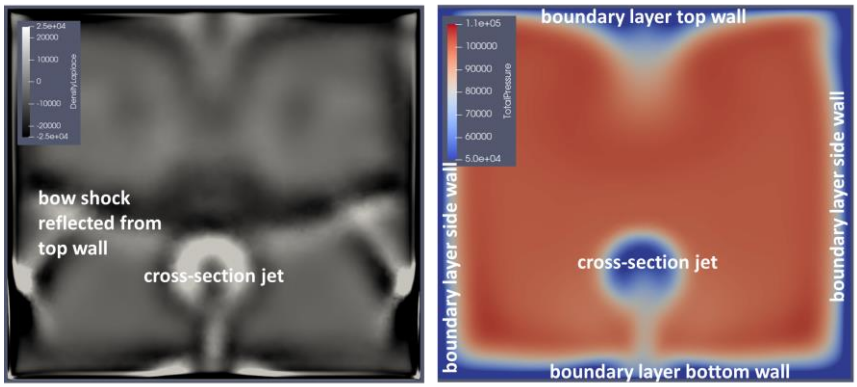

Fig 10. Left: Numerical shadowgraph image ($\nabla^2\rho$) flow in (y,z)-plane normal to free stream, at exit channel. **Right**: Computed distribution total-pressure in same plane. M_∞ = 1.6, J = 3.8 and S = 7.17

For M_∞ = 1.6, J = 3.8 and S = 7.17, Fig. 10 presents the numerical shadowgraph image ($\nabla^2\rho$) of the flow in the cross-sectional plane, normal to the free stream, close to the exit of the channel. It reveals the mushroom-shaped cross-section of the jet, as well as the reflection of the bow shock of the downstream jet into the top wall. The distribution of the total-pressure in the same plane, also shows the mushroom-shaped cross-section of the jet, with lower total pressure due to the flow passing through the barrel shock and the Mach disc. The boundary layer along the four walls is also evident as regions

with lower total pressure. Along the central part of the top wall the larger region with losses in total pressure is due to the flow passing through the stem of the Mach reflection of the bow shocks.
From the numerical Schlieren image in Fig. 9-left, created from the RaNS steady flow solution, the location of the upper shear layer of the jet can be clearly distinguished. The empirical scaling relation Eq. (1a), derived from Schlieren images in an earlier part of the study [19], superposed on Fig. 9 – left, correlates satisfactorily with the present results from RaNS.

Results Numerical Study – DDES

The results of the DDES time-resolved numerical simulation show an unsteady flow pattern containing features ranging over a large number of frequencies.

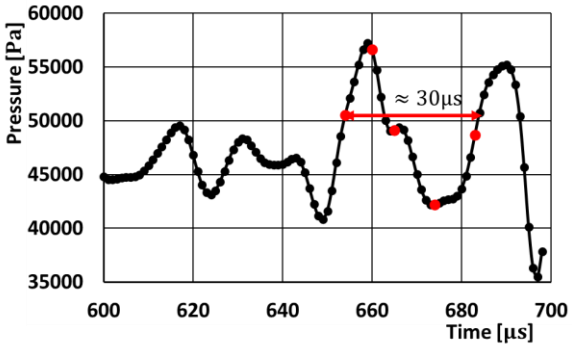

Fig 11. DDES: Time history pressure at probe positioned at $(x/D_t, 0, z/D_t)$ = (7.17,0.0,4.3), see Fig. 12, time step $1\mu s$. Results presented in Fig. 12 are data at 5 red dots in indicated period of 30 timesteps of $1\mu s$. Fig. 16 presents iso-incidence plots, one for 654(1)683 μs and one for 600(3)689μs. M_∞ = 1.6, J = 3.8 and S = 7.17.

Fig. 11 shows the history of the static pressure at a point (probe) just below the upper edge of the jet plume emanating from the main orifice, see third column Fig. 12. It indicates that one of the apparently occurring periods in the flow solution appears to be about $30\mu s$. For this period the numerical simulation, carried out with 1000 time-steps of $1\mu s$, is adequately time-resolved. For 5 discrete times in the period, indicated in Fig. 11 as red dots, Fig. 12 presents the flow solution as a numerical Schlieren image, a numerical shadowgraph and color plots of the magnitude of the vorticity and of the local Mach number. The numerical Schlieren images and the numerical shadowgraphs presented in Fig. 12 are quite similar to the wind-tunnel Schlieren images shown in Fig. 6. In the snapshots in Fig. 6 and in Fig. 12, as well as in videos of the computed time-dependent flow solution, similar shock patterns are evident, specifically, the two bow shocks, as well as their reflections in the top wall, associated with the two sonic jets emanating from the bottom wall of the test section. However, in Fig. 12, considered as the numerical counterpart of Fig. 6, many more details of the interaction of the two jets with the cross flow are evident, specifically when studied in combination with the pictures of the distribution of the magnitude of the vorticity $|\vec{\omega}|$ and of the Mach number. Moving from upstream to downstream one meets:
(**i**) The flow upstream of the first bow shock appears to be steady. Specifically, also in the bottom-wall boundary layer approaching the jet from the upstream orifice, the flow appears steady because in DDES the RaNS equations are solved there.
(**ii**) The so-called separation shock, upstream of the first bow shock, due to the interaction of the incoming boundary layer and this bow shock. The separation shock and the bow shock are clearly part of a λ-shock that forms on top of the incoming boundary layer.
(**iii**) Embedded within the subsonic-flow region on the downstream side of the normal part of the bow shock, one observes: (**a**) the tilted barrel shock with high-supersonic flow inside; (**b**) closed off by the Mach disc, and; (**c**) the region with lower-supersonic flow between the barrel shock and the upstream facing part of the mixing shear layer, which forms the contact between the fluid of the jet and that of the cross flow. This results in a weak secondary bow shock that develops just downstream of the most upstream bow shock. The foot of the secondary bow shock is attached to the Mach disc.
(**iv**) Downstream of the location of the Mach disc the jet plume from the upstream jet is supersonic, with a narrow subsonic-flow region (**a**) originating at the Mach disc. The flow inside this jet turns unsteady (**b**), evident from successive snapshots of Schlieren pictures in Fig.12 and from videos of the flow. Actually, in de videos it is observed that the t rigger is the subsonic (cross)flow around the Mach barrel becoming unsteady, similar to the subsonic flow around a cylinder perpendicular to the flow.

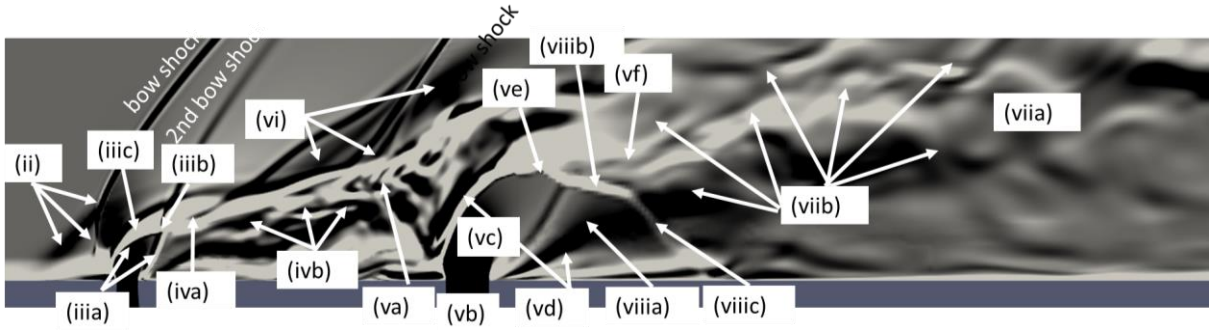

(**v**) Further downstream, the jet (**a**) from the first bottom-wall orifice interacts with the larger, main, jet emanating, at sonic speed, from the second bottom-wall orifice (**b**). This main jet, tilted by the cross flow, also features a high-supersonic flow inside its barrel shock (**c**), which is enclosed by a lower-supersonic flow between barrel shock and mixing shear layer(**d**), forming the interface between the fluid from the second jet and the surrounding fluid. The barrel shock is closed off by the Mach disc (**e**). In the second, main jet plume, the flow is, like the flow in the upstream jet plume, supersonic with a core (**f**) of subsonic flow of jet fluid that passed through the Mach disc.

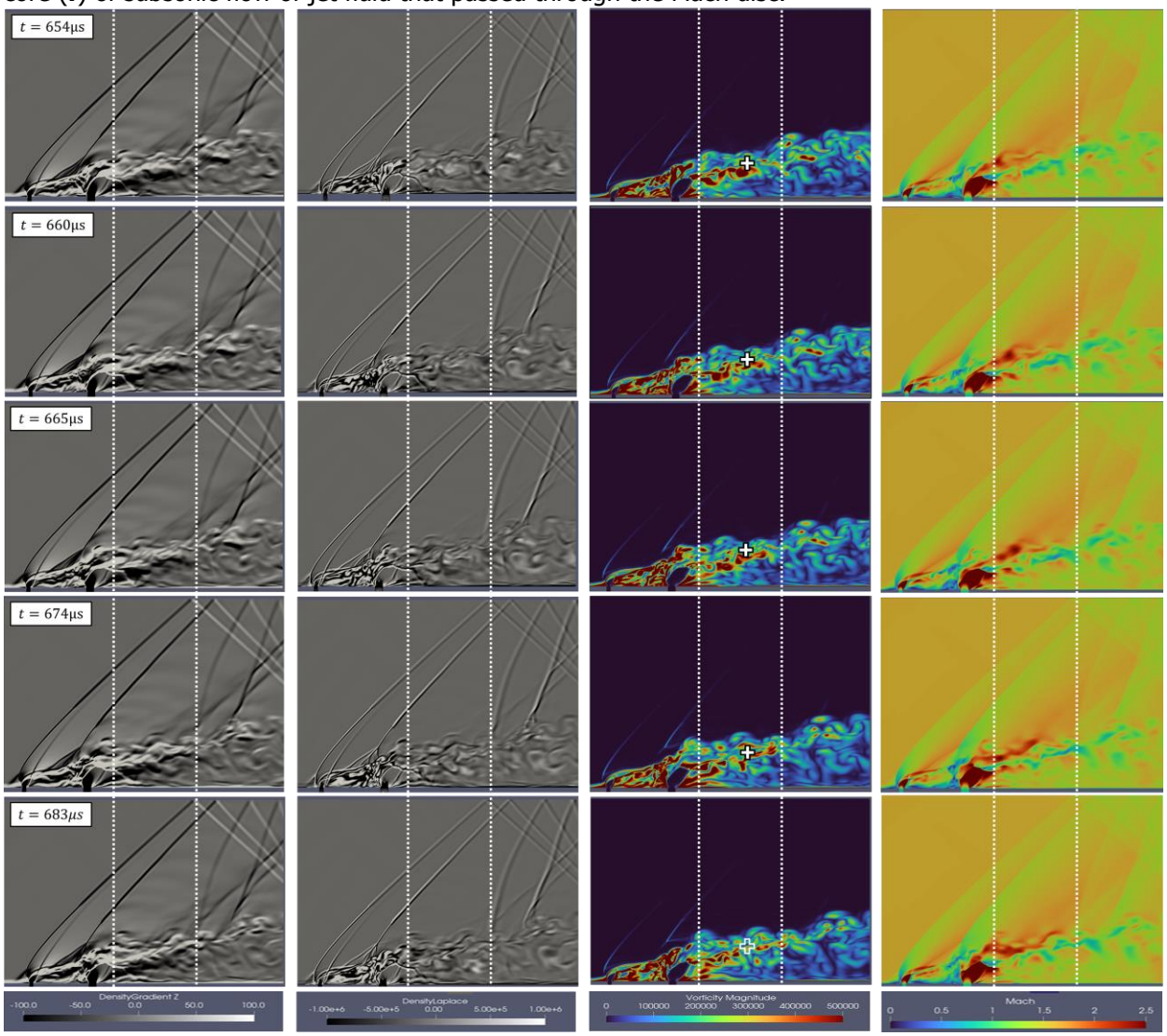

Fig 12. DDES flow solution in (x,z)-midplane at 5 points, successive in time, within a single period, see Fig. 11. From left-to-right: Numerical Schlieren image ($\partial\rho/\partial z$); Numerical shadowgraph image ($\nabla^2\rho$); Color plot magnitude vorticity ($|\vec{\omega}|$); Color plot Mach number; Vertical white dashed lines: reference lines; white open plus sign in plot with vorticity-magnitude: position of virtual pressure probe (Fig. 11). M_∞ = 1.6, J = 3.8 and S = 7.17

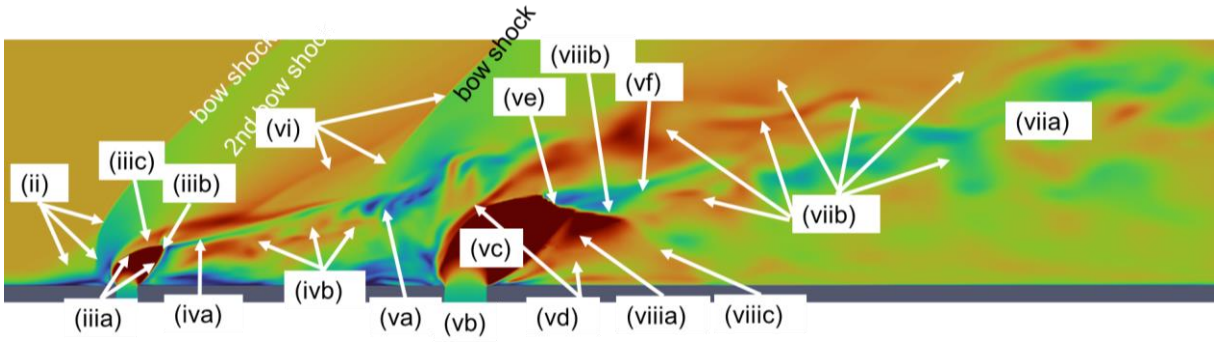

(**vi**) The jet from the upstream orifice causes the bow shock in front of the downstream jet to lift off and form a λ-shock on top of the jet plume from the first jet.
(**vii**) Downstream of the Mach disc of the second barrel shock, the plume of the jet from the second orifice develops as an unsteady supersonic flow with patches of subsonic flow (**a**). As clear from the numerical Schlieren pictures and shadowgraphs, but especially from the plot with the distribution of the magnitude $|\vec{\omega}|$ of the vorticity within the upper part of the plume, coherent vortical structures become visible in the jet plume. These vortical structures travel with the flow, i.e., in the images these structures (**b**), relative to the vertical dashed white lines, move downstream.
(**viii**) In the emanating main jet, on the downstream side of the barrel shock (**a**), the fluid from the jet enters the region between the barrel shock and the mixing shear layer where jet fluid mixes with cross-flow fluid. Here the flow, upwards along the barrel shock, is supersonic until at the position of the Mach disc, where a normal shock (**b**) slows down the fluid to subsonic speed in order to match up with the flow that passed through the Mach disc. Furthermore, the flow on the downstream side of the mixing layer, slightly supersonic, meets a normal shock (**c**) that slows down the flow to subsonic speed in order to match with the flow passing through normal shock (**b**).
(**ix**) In the numerical Schlieren images, immediately downstream of the second bow shock, more or less horizontal waves are distinguishable that travel to the top wall. These waves are caused by the unsteadiness in the first part of the upper shear layer of the main jet plume, i.e., the region where the jet plume from the first orifice collides with the upper shear layer of the main jet.
(**x**) The two primary bow shocks reflect at the (slip) upper wall of the test section through a regular reflection. The downwards reflected shocks do not interact with the main jet plume, at least not within the test section, see region below top wall in Fig. 12 left 2 columns.
(**xi**) Comparing RaNS results in Fig. 9 with DDES results in Fig. 12, makes clear that the interaction of the bow shocks with the boundary layer along the upper wall of the test section is different. In the case of RaNS, the reflection is through a Mach reflection, while in the case of DDES, with slip-conditions applied at the upper wall, the reflection is through a regular reflection.
(**xii**) In the numerical Schlieren images and numerical shadowgraphs, as well as in the Mach-number plot, another pair of shocks is discernible that do reflect on the main jet plume. These shocks have been identified as reflections of the primary bow shocks at the side walls, see Fig. 14.
(**xiii**) In the color pictures of the vorticity magnitude $|\vec{\omega}|$, vorticity is generated at the curved parts of the primary bow shocks, at the Mach discs, within the boundary layer along the bottom wall and at the mixing shear layers, where the fluid from the jet comes into contact with the cross-flow fluid.

Reliable results of wind-tunnel experiments are indispensable for the validation of mathematical models and of results of numerical simulations. However, compared to Schlieren wind-tunnel experiments, numerical flow simulations more easily provide data at locations not accessible in experiments. That has been exploited, for example, in Fig. 13, which shows results in the exit plane of the test section and Fig. 14, which presents results in a horizontal plane z = constant.
Fig. 13 presents, for the 5 points, successive in time within the selected cycle of the time-dependent DDES solution, the distribution of the x-component $\vec{\omega}.\vec{e}_x$ of the vorticity and the distribution of the total pressure, both on the exit-plane of the computational domain. In Fig. 13-top 2 types of vortical-flow regions are distinguished:
(a) vortical flow structures in the field, i.e., in the jet deflected by the cross-flow, and
(b) vortical structures in and near the bottom-wall boundary layer.

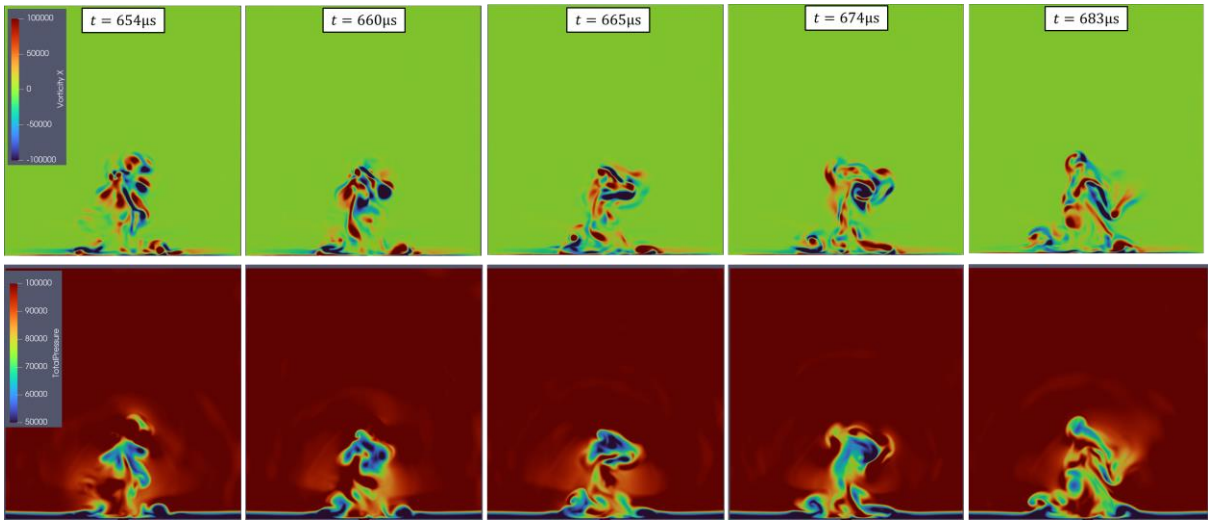

Fig 13. DDES flow solution in (*y,z*)-exit-plane at 5 points, successive in time, within a single period, see Fig. 11. **Top**: Color plot *x*-component vorticity ($\vec{\omega}.\vec{e}_x$), red: positive (counter-clockwise); blue negative (clockwise). **Bottom**: color plot total pressure [Pa]. M∞ = 1.6, J = 3.8 and S = 7.17

Ad (a): In the field, the mixing-promoting dynamics of the flow is evident. Vortical structures of positive (red: counterclockwise) and of negative (blue: clockwise) *x*-component of vorticity ($\vec{\omega}.\vec{e}_x$) interact with each other. In addition, the whole collection of vortical structures appears to sway from left to right.
When vortical structures are in close proximity there is a strong mutual interaction: two close vortical structures of the same sign rotate around their center of vorticity, while two close vortical structures of the same strength but of opposite sign, translate in the direction perpendicular to the line connecting their centers.
For the collection of vortical structures seen in the exit plane, its effect at some distant points from the collection, can be represented by a pair of counter-rotating vortical structures, a dipole. This corresponds to the mushroom-like cross-section of the jet plume, as evidenced in the RaNS solution in Fig. 10 and in the time-averaged DDES solution in Fig. 15b.
Ad (b): In the boundary layer along the bottom wall, the net effect of the presence of the field vortical structures results in an adverse pressure gradient in the direction of the flow induced by the field vorticity at the boundary layer. The latter induced flow is from the side walls to the midplane. This causes the boundary layer to separate, resulting in additional vortical structures, which interact mutually as well as with the vortical structures in the field.
Included in Fig. 13 are pictures of the distribution of the total pressure within the exit-plane. The results show that vortical structures and boundary layers cause losses in total pressure, and are often used to identify (strong) vortical structures and free or wall-bounded shear layers. Note that in Fig. 13, the boundary layers along the top wall and those along the side walls are absent: To save on grid points, in the present DDES computational study, slip boundary conditions haven been imposed along these walls, hypothesising that the boundary layers along these walls will not affect the development of the dual jets very much.

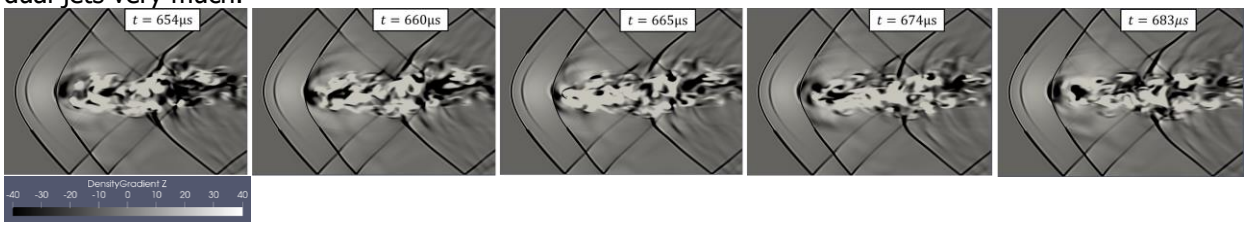

Fig 14. DDES flow solution in (*x,y*)-plane at 5 points, successive in time within a single period, see Fig. 11. Numerical Schlieren image ($\partial\rho/\partial z$) on cutting plane z/D_t = 4.47. M∞ = 1.6, J = 3.8 and S = 7.17

Fig. 14 presents, again for the 5 successive points in time within the selected cycle of the time-dependent DDES solution, numerical Schlieren snapshots on the plane z = 4.47D_t, a cutting plane that is parallel to the bottom wall at a distance just above the two barrel-shocks. The plane, cuts through the bow shocks and their reflections at the (slip) side walls. The plane also cuts through the main jet plume.

Most of the flow features identified in the mid plane in Fig. 12 show up in Fig. 14, which provides useful insight in the flow field in lateral direction.
(**i**) The first, upstream, primary bow shock, as well as the second primary bow shock, is well-resolved, with an increase in shock thickness about halfway to the side walls. At that location, the apparent thickening is due to the grid becoming less fine towards the side walls.
(**ii**) The lateral extent of the weaker secondary bow shock, that forms just downstream of the first primary bow shock, is clearly visualised.
(**iii**) The horizontal cutting plane intersects the second bow shock just below the merging point of the two legs of the λ-shock, evidenced by the blackish area immediately upstream of the second primary bow shock.
(**iv**) At the (slip) side walls, the two primary bow shocks show a regular reflection, not a Mach reflection with a Mach stem. The reflected shocks hit and interact with the unsteady flow inside the main jet plume. Subsequently these shocks reflect and continue their path, back towards the side walls, where they reflect once more.
(**v**) The flow topology is mostly stationary, except in the main jet plume, where the mixing takes place.

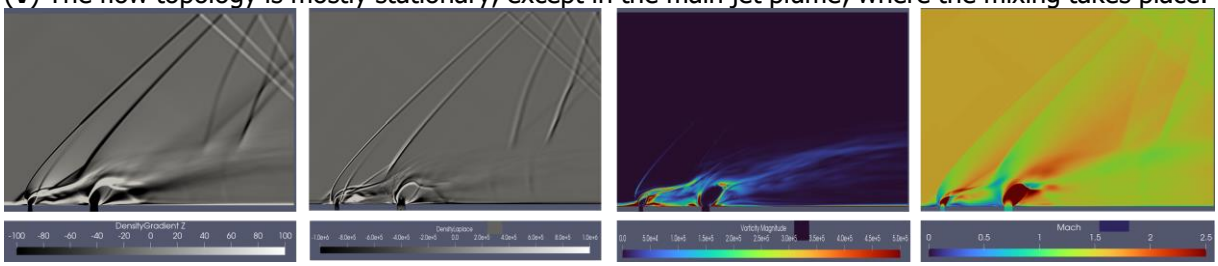

Fig 15a. DDES: Time-averaged (over 1000 time-steps of 1μs) flow solution in (x,z)-midplane. From left-to-right: Numerical Schlieren image ($\partial\rho/\partial z$); Numerical shadowgraph image ($\nabla^2\rho$); Color plot magnitude vorticity ($|\vec{\omega}|$); Color plot Mach number. M_∞ = 1.6, J = 3.8 and S = 7.17

Figs. 15a presents, for the (x,z)-midplane, the time-dependent DDES solution, but now time-averaged over the 1000 time-steps of 1μs carried out in the numerical simulation. Like in Fig. 12 four types of plots are shown: numerical Schlieren image, numerical shadowgraph, vorticity magnitude ($|\vec{\omega}|$) color plot and color plot with the distribution of local Mach number. Comparing any row of images in Fig. 12 and the row of plots in Fig. 15a learns that the shock wave pattern, including the λ-shock at the foot of the two primary bow shocks, the reflections at the walls, as well as the barrel shocks are grossly stationary. The internal detailed dynamics of the jet plumes of the dual-jet injection, evident in Fig. 12, has been averaged out within the envelope of the jet plumes.
The RaNS solution, presented in Fig. 9 as a numerical Schlieren image, though obtained on a coarser grid than the DDES grid, correlates well with the time-averaged DDES results presented in Fig. 15a.

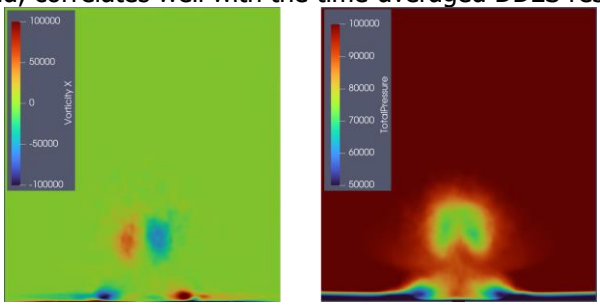

Fig 15b. DDES: Time-averaged (over 1000 time-steps of 1μs) flow solution in (y,z)-exit-plane. **Left**: color plot x-component vorticity ($\vec{\omega}.\vec{e}_x$), red: positive (counter-clockwise), blue: negative (clockwise). **Right:** color plot total pressure. M_∞ = 1.6, J = 3.8 and S = 7.17

Fig. 15b presents, for the (y,z)-exit plane, the time-dependent DDES solution, but now time-averaged over the 1000 time-steps carried out in the numerical simulation. Like in Fig. 13, two plots are shown: (1) a color plot of the distribution of the x-component of vorticity ($\vec{\omega}.\vec{e}_x$) and (2) a color plot of the distribution of the total pressure. Comparing any image in the upper row of pictures in Fig. 13 and the left image in Fig. 15b shows that, though the time-dependent distribution of $\vec{\omega}.\vec{e}_x$ in Fig. 13 is not left-right symmetric at all, that the time-averaged distribution of $\vec{\omega}.\vec{e}_x$ in Fig. 15b is, nearly perfect, left-right symmetric. This is also true for the distribution of the total pressure. Fig. 15b nicely shows the

cross-section of the jet plume as a mushroom-like structure with positive $\vec{\omega}.\vec{e}_x$ on the left and negative $\vec{\omega}.\vec{e}_x$ on the right. This structure, as well as the secondary vortical structures at the bottom wall, are stationary. This because of the nearby presence of the lower wall, in effect causing the presence of a virtual, mirror-imaged, vortical structure below the wall, such that the zero-normal-velocity boundary condition is satisfied at the (no-slip) wall.

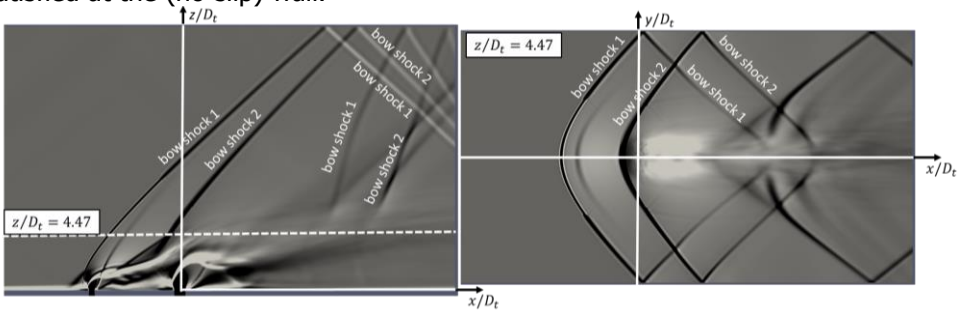

Fig 15c. DDES: Time-averaged (over 1000 time-steps of 1μs) flow solution, numerical Schlieren image ($\partial\rho/\partial z$). **Left:** in (x,z)-midplane (repeated Fig. 15a); **Right**: in (x,y)-cutting-plane z/D_t = 4.47. M$_\infty$ = 1.6, J = 3.8 and S = 7.17

Fig. 15c presents, for the (x,y)-cutting plane z/D_t = 4.47, the time-dependent DDES solution, now time-averaged over the 1000 time-steps carried out in the numerical simulation, producing the numerical Schlieren image Fig. 15c-right. For ease of orientation, Fig. 15c-left repeats the most-left numerical Schlieren image of Fig. 15a, i.e., showing the time-averaged solution in the (x,z)-midplane. Comparing any image in Fig. 14 and the image Fig. 15a-right, learns that the shock pattern, including the reflected shocks at the side walls, is largely stationary. However, the internal details of the main jet plume have disappeared in the averaging operation, leaving the envelope of the jet plume as a (positive-y)/(negative-y)-symmetric area.

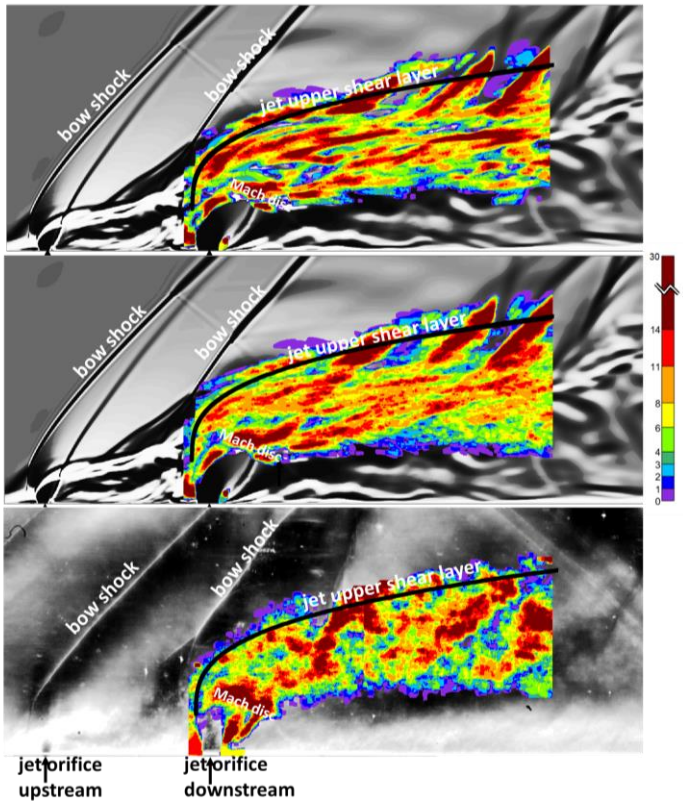

Fig 16. Iso-incidence plot obtained from numerical Schlieren images ($\partial\rho/\partial z$) generated from time-dependent DDES solution. **Top:** 30 consecutive snapshots between 654μs and 683μs; **Middle**: 30 consecutive snapshots between 600μs and 689μs, see Fig. 11. **Bottom:** 30 consecutive wind-tunnel Schlieren images within period of 30ms (copy of Fig. 7). Scale on right gives iso-incidence values. **Solid curves**: similarity expression for time-averaged location upper edge jet shear layer, Eq. (1a). Coefficient of determination R^2= 0.80 for top and middle plot. R^2= 0.74 for bottom plot

To analyse the numerical results use has been made of numerical Schlieren images, typical for the investigation of flows in wind tunnels (as well as in flight experiments). The post-processing procedure for Schlieren images obtained in experiments has also been applied to the numerical Schlieren images. The procedure is the largely automated, post-processing procedure, developed by Smink [11], e.g., see the iso-incidence plot in Fig. 7, repeated at the bottom of Fig. 16. The two upper iso-incidence plots in Fig. 16 have been generated from the numerical Schlieren images obtained from the DDES flow solution, with 30 consecutive images as input, see Fig. 11:
(a) the top plot in the range 654μs to 683μs, selecting all 30 numerical Schlieren images available;
(b) the bottom plot in the larger range 600μs to 689μs, selecting consecutive images every 3 μs.
In the iso-incidence plot, the color at a specific location in the jet plume indicates the incidence, i.e., the number of times a feature is present at a certain place. The iso-incidence plot reveals either largely stationary, or frequently-occurring, flow structures.
Ad (a): The top plot reveals that, within one period of the unsteady flow, the jet plume consists of 4 parallel, streamwise, streaks at different heights within the plume, consisting of a sequence of features along the plume of the jet. In the shown part of the jet plume, of length of about two distances between the orifices, i.e., $2\Delta x$, the distance between individual features appears to be about $0.5\Delta x$, i.e., half the distance between the orifices. These streaks reveal the unsteady inner structure of the jet. The other dominant structures at the upper boundary of the jet plume, near the end of the shown area, are interactions of the jet plume with the bow shocks reflected from the side walls. These reflected shocks are identified in Figs. 14c and 15c.
Ad (b): The middle plot reveals that, in the iso-incidence plot constructed from 30 successive images taken during a longer period of time (90μs), the jet plume also appears to consist of streaks, with a non-periodic appearance of the location of flow features in the streaks.
The empirical similarity relation, given in Eq. (1a), for the time-averaged location of the upper shear layer of the jet plume, derived from physical Schlieren images obtained in the wind tunnel and the location obtained from DDES and the one obtained from RaNS correlate quite well, for the conditions (S,J) = (3.8,7.17) considered in the present study.

Conclusions

- The Schlieren images from the experimental study have been utilized to investigate dual, tandem, sonic jet injection, normal to the supersonic cross flow of Mach 1.6. This resulted in an empirical scaling relation of the time-averaged location of the upper shear layer of the jet, i.e., the penetration depth of the dual-jet injection. For J-dependent intermediate values of S, i.e., dimensionless distance between the two orifices, the upstream jet imposes a shielding effect on the downstream jet, which results in an enhanced penetration depth of the upper shear layer of the jet plume from the main, downstream, orifice.
- The numerical study illustrates that the computational results of RaNS and the time-averaged ones of the time-accurate DDES match the results derived from the experiments: for the selected test case (S,J) = (3.8,7.17) numerical Schlieren images and penetration depth are very similar.
- The post-processing procedure developed for extracting iso-incidence plots from wind-tunnel Schlieren images and determine the penetration depth of the main jet plume, has also found fruitful application in processing numerical Schlieren images.
- The numerical results, specifically the time-accurate ones from DDES are clearly very powerful in enabling a thorough analysis of the complex flow field of dual-jet injection in a supersonic cross flow. The numerical results reveal many details in the way the jet plume from the main orifice is affected by the shielding flow field induced by the jet emanating from the upstream orifice.
- Future work: Numerical simulations with DDES for additional conditions in the (S,J)-parameter plane and for other Mach numbers M_∞; Improvement wind-tunnel Schlieren system and carrying out wind-tunnel experiments at further conditions in the (S,J)-parameter plane and for other Mach numbers M_∞; Exploration of using Wall Modelled LES (WMLES), in order to validate the transient behavior observed in the numerical simulations carried out with DDES in the present study; Derivation of a measure for the efficiency of the mixing in relation to the loss in total pressure.

Acknowledgements

The authors acknowledge W. Lette, S. Wanrooij, H. Stobbe, E. Leusink, L. Tiemersma and F.B. Segerink for their contributions in the wind-tunnel experiments. M. Wilens for his contribution in the numerical part of the study. TNO is thanked for their cooperation in the realisation of this paper.

References

1. Roberts, K.N.: Analysis and Design of a Hypersonic Scramjet Engine with a starting Mach number of 4.00. PhD thesis, The University of Texas at Arlington (2008)
2. https://en.wikipedia.org/wiki/Scramjet, assessed October 10 2019
3. Landsberg, W.O., Wheatley, V., Veeraragavan, A.: Characteristics of cascaded fuel injectors within an accelerating scramjet combustor. AIAA Journal, Vol. 54, No. 12, pp. 1–9 (2016). DOI: 10.2514/1.J054815
4. Tanimizu, K., Mee, D.J., Stalker, R.J., Jacobs, P.A.: Nozzle design study for a quasi-axisymmetric scramjet-powered vehicle at Mach 7.9 flight conditions. Shock Waves, Vol. 23, No. 5, pp. 453–460, (2013). DOI: 10.1007/s00193-013-0449-4
5. Lee, J.: Numerical study of mixing in supersonic combustors with hyper-mixing injectors. Journal of Propulsion and Power, Vol. 10, No. 3, May-June 1994
6. Lee, S.-H.: Characteristics of dual transverse injection in scramjet combustor, part 1: Mixing. Journal of Propulsion and Power, Vol. 22, No. 5, pp. 1012–1019 (2006) https://doi.org/10.2514/1.14180
7. Giskes, E., Verschoof, R.A., Segerink, F.B., Venner, C.H.: Schlieren study of a sonic jet injected into a supersonic cross flow using high-current pulsed LEDs. arXiv:1606.06683 (2016).
8. Settles, G.S.: Schlieren and Shadowgraph Techniques. Springer (2001)
9. De Maag, S., Hoeijmakers, H.W.M., Venner, C.H., Segerink, F.B., Offerhaus, H.L.: Power VCSEL driven Schlieren visualization for cascaded injection in supersonic flow. In Proceeding (e-book) 15th International Conference on Fluid Control, Measurements and Visualization, 27-30 May 2019, Naples, Italy (2019). https://flucome2019.unina.it/e-book/FLUCOME2019.html
10. De Maag, S., Hoeijmakers, H.W.M., Venner, C.H., Segerink, F.B., Offerhaus, H.L.: Investigation of tandem injection in supersonic flow using Schlieren visualization. AIAA Paper 2020-0040
11. Smink, J.S., Hoeijmakers, H.W.M. and Venner, C.H.: Investigation of behavior jet shear layer in tandem dual jet injection in supersonic cross flow from Schlieren images. AIAA Paper 2022-2565. Published as AIAA Journal, Vol.60, No. 11, November 20, 2022, pp. 6277-6288. https://doi.org/10.2514/1.J061843
12. Palacios, F., Colonno, M.R., Aranake, A.C., Campos, A., Copeland, S.R., Economon, T.D., Lonkar, A.K., Lukaczyk, Taylor, T.W.R., and Alonso, J.: Stanford University Unstructured (SU2): An open-source integrated computational environment for multi-physics simulation and design. In 51st AIAA Aerospace Sciences Meeting including the New Horizons Forum and Aerospace Exposition. AIAA Paper 2013-0287, 2013
13. Economon, T.D., Palacios, F., Copeland, S.R., Lukaczyk, T.W. and Alonso, J.J.: SU2: An Open-source suite for multiphysics simulation and design. AIAA Journal, Vol. 54, No. 3, March 2016. https://doi.org/10.2514/1.J053813
14. Spalart, P.R., Jou, W.-H., Strelets, M. and Allmaras R.S.: Comments on the feasibility of LES for wings, and on a hybrid RANS/LES approach. 1st AFOSR Int. Conf. on DNS/LES, Aug. 4-8, 1997, Ruston, LA. In "Advances in DNS/LES", C. Liu and Z. Liu Eds., Greyden Press, Columbus, OH, 1997
15. Spalart, P.R, Deck, S., Shur, M.L., Squires, K.D. Strelets, M.K. and Travin, A.: New version of detached-eddy simulation, resistant to ambiguous grid densities. Theoretical and Computational Fluid Dynamics, 20(3):181–195, 2006
16. Spalart, P.R. and Allmaras, S.R.: A one-equation turbulence model for aerodynamic flows. La Rech. Aerospatiale 1, 5-21, 1994
17. Wang, Z.J.: A fast nested multi-grid viscous flow solver for adaptive Cartesian/Quad grids. Int. J. Numer. Meth. Fluids, Vol. 33, pp. 657–680, 2000
18. Ayachit, U.: The ParaView Guide: A Parallel Visualization Application, Kitware, 2015, ISBN 9781930934306
19. Smink, J.S., De Maag, S., Lerink, C.W., Giskes, E., Hoeijmakers, H.W.M., Venner, C.H., Segerink, F.B., Offerhaus, H.L.: Schlieren Visualization of Dual Jet Injection in Supersonic Cross flow" Proceedings HiSST 2nd International Conference on High-Speed Vehicle Science Technology, Bruges, Belgium, September 11 - 15, 2022, 14 pages. HiSST2022 Best Overall Paper Award.